Spatial Intensity Distribution in Plasmonic Particle Array Lasers

Ke Guo and A. Femius Koenderink*

Center for Nanophotonics, AMOLF, Science Park 104, 1098XG Amsterdam, The Netherlands

(Received 31 May 2018; revised manuscript received 22 December 2018; published 11 February 2019)

We study spatial intensity distributions in plasmonic distributed feedback lasers (DFB) composed of metal nanoparticle arrays. Real-space distributions give direct access to "coupling-strength" parameters that quantify DFB performance in the framework of coupled-wave theory (CWT). We observe that CWT indeed parametrizes real-space intensity distributions and extract coupling-strength parameters that quantify the plasmonic feedback mechanism. These coupling-strength parameters differ from those required to parametrize the plasmonic band structures of the system, counter to the common result for dielectric DFB lasers, where CWT describes both real-space and *k*-space physics. Also, the measured coupling constants are significantly smaller than would be expected from estimates on the basis of the unit-cell geometry. We conclude that while CWT is successful as a generic description of any system with forward and backward waves with gain, matching this model to photonic band structures, or to common parameter-estimate approaches, fails because the underlying assumption that a perturbative plane-wave expansion applies is not valid for plasmonic antenna arrays.

DOI: 10.1103/PhysRevApplied.11.024025

I. INTRODUCTION

Currently there is great interest in collective light-matter interaction effects in periodic resonant scattering systems, such as plasmonic antenna arrays and dielectric metasurfaces [1]. Diffractive plasmonic antenna arrays provide strong field confinement, owing to the plasmonic nature of the constituent scatterers in the unit cell, yet compared to single-plasmon nanoantennas they yield higher quality factors and concomitantly lower absorption losses. As reviewed by Lozano *et al.* [2], this poses significant advantages for solid-state lighting. Recently, several groups have noted that such structures are also of considerable interest for effects beyond fluorescence control (cooperative emission), including plasmon antenna array lasers [3–16], strong coupling between dense emitter ensembles and plasmon antenna arrays [17,18], plasmon-exciton-polariton lasing [13], and Bose-Einstein condensation of exciton-polaritons [19]. In a separate development, there is a rising level of interest in dielectric lasing metasurfaces with resonant building blocks as lossless alternatives to plasmonic arrays [20]. In all these efforts, there is a great need to quantitatively understand the emergence of cooperative emission, accounting at the same time for the periodicity, the strongly resonant properties of the unit cell, and finite-sized effects in finite system realizations. Currently, this is far beyond standard numerical approaches. For instance, full-wave numerical approaches for plasmon systems are only feasible either with periodic boundary conditions (full unit-cell resolution, no finite-system effects) or for real-space domains that are too small to encompass a realistic number of system unit cells (a finite system, but hardly recognizable as periodic).

In this work, we focus on plasmon antenna array lasers, which are the most well studied example of the above-mentioned systems. Diffractive plasmon lasers [3–16] were first considered as potential realizations of the plasmon spaser [21] with a better tradeoff [22] between confinement and loss than single-nanoparticle or -nanowire realizations [23–34]. Diffractive plasmonic structures with gain are akin to distributed feedback (DFB) lasers [35–40]. Lasing of these systems occurs near geometric Bragg conditions and is strongly directional, with thresholds similar to those of polymer DFB lasers. At the same time, they have much larger interaction strength than conventional dielectric DFB lasers owing to the strong resonant scattering cross section of plasmon antennas. This is apparent in the wide stop gaps measured in plasmon-lattice band structures [41]. To understand such plasmon antenna array lasers, Odom's group has notably focused on Purcell enhancement due to strong field confinement [8–11], which is particularly relevant for intrinsically low quantum-efficiency-gain media. In a different realization using efficient instead of inefficient dyes, Schokker *et al.* [42] have claimed that plasmon particle array lasers also stand out for strong feedback from resonant scattering, which makes them extraordinarily robust to disorder. While the underlying plasmon band structure in both these realizations was studied in depth, these works did not address, quantitatively in real space, how particle array

*f.koenderink@amolf.nl

plasmon lasers compare to conventional DFB lasers based on dielectric or loss and/or gain gratings.

In this paper, we study finite-sized plasmon particle array lasers and quantitatively compare their properties to coupled-wave predictions. As these lasers are qualitatively akin to DFB lasers in their characteristics, our aim is to examine whether the coupled-wave theory (CWT) developed by Kogelnik and Shank [43] can offer an accurate description of these systems and therefore form a strong basis to describe active plasmonic and resonant dielectric metasurfaces and cooperative phenomena in plasmon antenna arrays beyond lasing. Good agreement between CWT and experiments has been demonstrated for metal hole array lasers [4,5], which, however, have weak and nonresonant perturbations (the air holes). To benchmark whether this premise also holds for resonant antenna array systems, it is important to perform quantitative instead of qualitative comparisons. In this work, we determine coupling strengths from measured spatial intensity distributions of lasing modes in plasmon particle arrays as a function of the detuning of the lasing condition from the particle plasmon resonance. By comparing fitted coupling strengths with calculations and measured band structure parameters, we answer two questions: (i) whether the CWT meant for weakly scattering systems applies to plasmonic lattices in terms of parametrizing spatial intensity distributions and, if so, (ii) how the plasmon resonance near the lasing condition influences the apparent coupling strength and the band structure.

II. CWT FOR DFB LASERS

This section summarizes those aspects of CWT required to describe our experiments. CWT was developed by Kogelnik and Shank in 1972 to describe one-dimensionally periodic DFB lasers [43] and was later further extended to different one-dimensional (1D) and two-dimensional (2D) DFB laser geometries [44–47]. In CWT, a DFB laser is described as a waveguide with a weakly scattering periodic perturbation in its optical constant, which leads to coupling between forward- and backward-propagating in-plane waves [43,44] by Bragg diffraction. Furthermore, these waves experience gain and are subject to outcoupling loss, also due to Bragg diffraction. Reported plasmon-lattice lasers are usually 2D periodic structures, with resonant nanoantennas assembled in a 2D lattice. To derive CWT for 2D systems, the starting point is a plane-wave expansion method to solve for the in-plane amplitude distribution of modes that are understood to have a vertical mode profile and mode index n_{WG}, taken from the uncorrugated 2D waveguide solution. The periodic corrugation is incorporated as a small perturbation that couples the waves through coupling constants $\kappa(\mathbf{G})$, where the set $\mathbf{G}$ refers to the reciprocal lattice vectors. The coupling constants are determined by the 2D Fourier transform of the unit-cell corrugation, weighted with the finite overlap of the vertical waveguide mode profile [44]. For our system, the coupling constants have complex values. Real and imaginary coupling constants are commonly understood for DFB lasers as index coupling and gain (or loss) coupling, respectively.

While, in principle, periodic potentials couple all plane-wave components of any ansatz solution written as a Bloch-wave expansion, the essence of CWT is that only a small subset of plane waves and $\mathbf{G}$ values need to be considered, namely only those that allow standing waves by Bragg diffraction. Following the model for 2D lattices presented in Ref. [45], this means only those waves with in-plane momentum $|\mathbf{k}+\mathbf{G}| = \omega/cn_{\mathrm{WG}} = \beta$, with an optical frequency ω in the gain window of our lasing medium, and close to a Bragg condition should be retained. Here "close" means within a few times the frequency bandwidth of the stop gap associated with lasing, which is a few percent wide for plasmon-lattice lasers [48]. The philosophy of our work is to extract coupling constants κ by comparing measured spatial intensity profiles that are predicted by CWT. Since for square lattices the predicted profiles are quite complex [45], we focus on 2D arrays with a rectangular geometry instead of a square geometry. The pitches a_x and a_y are designed to be different by about 15%, such that the Bragg conditions in the x and y directions cannot be simultaneously met and only the waves in the y direction couple within the narrow frequency window of the laser gain. Retaining only those Bragg conditions, the 2D model reduces to the 1D CWT equations, with the coupling coefficients κ calculated from the 2D unit-cell geometry. The light field is reduced to the sum of two counterpropagating waves $S(y)e^{iG_y y}$ and $R(y)e^{-iG_y y}$ traveling in the $-y$ and y directions that are coupled through the first- and second-order Bragg diffractions [Fig. 1(a)]. Lasing operation is expected near the second-order Bragg diffraction, at a wave vector near $G_y = 2\pi/a_y$, where a_y is the lattice constant in the y direction. The slowly varying envelopes $R(y)$ and $S(y)$ satisfy [44]

$$-\partial_y R(y) + \left\{\frac{g}{2} - \frac{i}{2G_y}\left[n_{\mathrm{WG}}^2\left(\frac{\omega}{c}\right)^2 - G_y^2\right] - \kappa_{\mathrm{out}}\right\} R(y) - (i\kappa_{\mathrm{back}} + \kappa_{\mathrm{out}})S(y) = 0, \tag{1a}$$

$$\partial_y S(y) + \left\{\frac{g}{2} - \frac{i}{2G_y}\left[n_{\mathrm{WG}}^2\left(\frac{\omega}{c}\right)^2 - G_y^2\right] - \kappa_{\mathrm{out}}\right\} S(y) - (i\kappa_{\mathrm{back}} + \kappa_{\mathrm{out}})R(y) = 0. \tag{1b}$$

Here, κ_{back} quantifies the coupling strength responsible for feedback through second-order Bragg diffraction [$\mathbf{G} = (0, 4\pi/a_y)$] and κ_{out} that for the coupling between guided waves and out-of-plane radiation through first-order Bragg diffraction [$\mathbf{G} = (0, 2\pi/a_y)$]. We further define $\kappa = \kappa_{\mathrm{back}} - i\kappa_{\mathrm{out}}$.

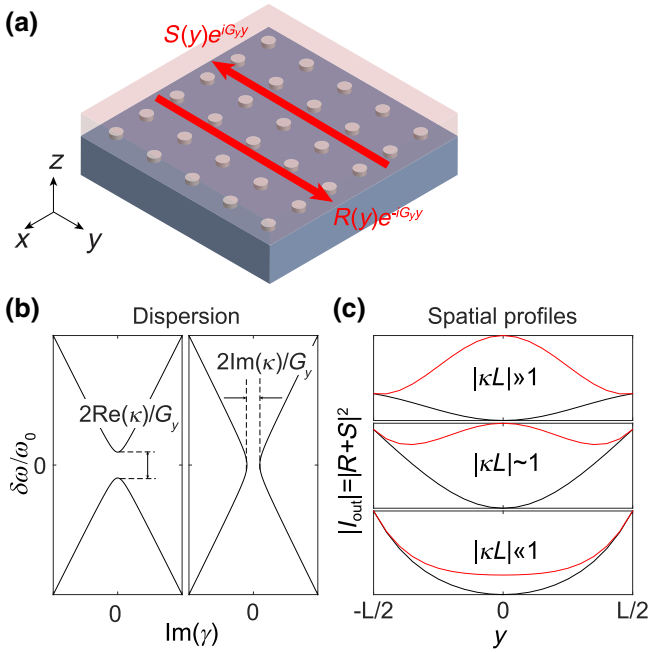

FIG. 1. (a) A sketch of a plasmon DFB laser based on a rectangular lattice of Ag nanoparticles. Feedback only occurs in the y direction (b) canonical photonic band diagram of CWT, with $\kappa_{\mathrm{back}} \gg \kappa_{\mathrm{out}}$. The real (imaginary) part of the coupling coefficient results in a band gap in frequency (a wave vector). (c) Canonical intensity profiles of the outcoupled lasing mode (the lowest threshold) in undercoupled, critically coupled, and overcoupled regimes (bottom to top). Red (black) indicates the (anti)symmetric combinations $|R \pm S|^2$.

Following Refs. [43,44], the above equations provide the below-threshold band structure and the above-threshold real-space intensity distribution. Figure 1(b) illustrates two typical types of below-threshold band structures. The coupling between the two waves opens a band gap at the crossing of the two waveguide modes at $k_y = 0$ and $\omega_0 = cG_y/n_{\mathrm{WG}}$. When $|\mathrm{Re}\,\kappa| \gg |\mathrm{Im}\,\kappa|$, the photonic bands split at $k_y = 0$ with a gap in frequency, with $\delta\omega = \omega - \omega_0 \approx \frac{\omega_0}{G_y}(-i\kappa_{\mathrm{out}} \pm \kappa)$. The stop gap is symmetric around the Bragg condition ω_0 as long as $|\kappa_{\mathrm{back}}| \gg |\kappa_{\mathrm{out}}|$, i.e., unless the radiation loss is strong [Fig. 1(b, left)]. If $|\mathrm{Re}\,\kappa| \ll |\mathrm{Im}\,\kappa|$ (gain or loss coupling), the photonic bands split in wave vector rather than in frequency, as shown in Fig. 1(a, right).

The above-threshold real-space profiles have the following form (overall array dimension L):

$$R(y) = \sinh\gamma\left(y + \frac{1}{2}L\right) \quad \text{and}$$
$$S(y) = \pm\sinh\gamma\left(y - \frac{1}{2}L\right), \tag{2}$$

where γ and the threshold gain g_{thr} satisfy

$$\pm i\gamma/\sinh\gamma L = \kappa \quad \text{and} \quad g_{\mathrm{thr}} = 2\mathrm{Re}(\gamma\coth\gamma L + \kappa_{\mathrm{out}}). \tag{3}$$

The slowly varying envelopes determine the output spatial intensity distribution obtained when imaging the laser with far-field optics. In a purely scalar model, the intensities of the two waves outcoupled by the lattice through the first-order Bragg diffraction add up as $|R+S|^2$. Once polarization is included in the model, for samples supporting a transverse electric (TE) [respectively transverse magnetic (TM)] waveguide mode, it is important to realize that detection polarization along x [respectively y] selects $|R+S|^2$, while cross-polarized detection results in a signal proportional to $|R-S|^2$.

Figure 1(b) shows examples of $|R+S|^2$ for various combinations of the array size L and the coupling constant κ. Depending on the sign in Eq. (2), the outcoupled waves present either constructive or destructive interference, resulting in bright (antinodes on the particles) and dark (nodes on the particles) modes. Dark modes (the black lines) have zero emission intensity in the center of the array and yet high intensity on the edges. A bright mode (the red lines) has a spatial profile that is dependent on the product of the coupling strength κ and the overall array size L, which can be classified into three regimes: undercoupled, critically coupled, and overcoupled. When $|\kappa L| \ll 1$ (undercoupled), the emission profile of the first lasing mode will essentially report on the sinh tails in Eq. (2), meaning bright emission only from the array edges. As $|\kappa|$ increases, the laser transitions from critically coupled to overcoupled ($|\kappa L| \gg 1$) and the emission in the center increases.

To conclude, CWT simultaneously predicts below-threshold photonic dispersion diagrams with characteristic stop gaps and above-threshold real-space intensity distributions, both parametrized by the *same* coupling-strength parameters κ. These parameters should be expected to systematically vary with the plasmon particle resonance. In this spirit, we seek to determine the relation between the coupling strength (κ) and the plasmon response from spatial intensity distributions for different array sizes (varying L) and particle sizes.

III. EXPERIMENTAL SETUP AND SAMPLE GEOMETRY

We perform measurements in an inverted fluorescence microscope equipped with real-space and back focal plane (Fourier-space) imaging, as well as spectral (Fourier) imaging, using a modified version of the setup of Ref. [12] [cf., Fig. 2(a)]. To obtain a large field of view, we use a Nikon L PLAN, 50×, NA = 0.7 objective. We pump and collect through the substrate side, employing single 532-nm-wavelength, 0.5 ps pulses (Teem Photonics,

type STG-03E-1S0), with a beam diameter of approximately 120 μm on the sample and a pulse energy up to approximately 1 μJ. The pulse energy is controlled by an acousto-optic modulator (AOM). To avoid any polarization anisotropies, we convert the pump polarization to circular and use a beam splitter ($R = 80\%$) as opposed to a dichroic mirror. Emission is collected through the beam splitter, passed through a pair of Chroma HHQ545lp longpass filters to remove pump light, and directed through a 1× telescope to either a thermoelectrically cooled Si charge-coupled device (CCD) camera (Andor CLARA) or a Shamrock303i spectrometer (with Andor iVAC Si CCD) after tube lens of 200 and 100 mm, respectively. The first telescope lens counted from the sample is placed at its focal distance from the back focal plane of the objective and also works as a Fourier or "Bertrand" lens when the second lens of the telescope is removed. When the back focal plane of the objective is imaged on the spectrometer, the entrance slit (20 μm) selects a vertical slice in the center of the Fourier image ($k_x = 0$) so that the emission intensity as a function of k_y and ω is imaged on the spectrometer camera. As demonstrated by Schokker [12], the resulting spectral images show distinct features that trace out the band structure of the sample, when operated below threshold. Similarly, in real-space imaging, the spectrometer slit (slit width 20 μm) spatially selects a strip of width 0.8 μm on the sample. Above threshold, these techniques provide the lasing spectrum and the spatial distribution of the lasing modes.

The arrays are designed to have a lattice constant of 370 nm in the y direction. In the x direction, the array has a much smaller lattice constant of 320 nm. Since this pitch is 15% shorter than the y pitch, the corresponding Bragg conditions are far away from the stop gap relevant for lasing (almost 100 nm, versus a stop-gap width < 10 nm). In fact, Bragg diffraction in the y direction only occurs at 490 nm wavelength, not just outside the dye gain window but even well to the blue of the pump wavelength. Therefore, only the waveguide modes in the y and $-y$ directions can couple with each other through the Bragg diffraction of order (0,2), while outcoupling occurs through the Bragg diffraction of order (0,1). As other diffraction orders do not contribute, the lasing action is essentially as in a 1D periodic DFB laser. The Ag nanoparticles are fabricated on glass cover slips using electron-beam lithography, successive thermal evaporation, and lift-off [12]. Each Ag nanoparticle has a height of 30 nm and a diameter that we systematically vary from 40 to 90 nm in different arrays. The samples are covered by spin coating a 350 nm SU8 layer doped with about 2.5 wt % Rh6G molecules, which acts as both a gain medium and a waveguide layer. Because SU8 has a refractive index of about 1.60 (measured by ellipsometry), exceeding the index of the glass substrate ($n = 1.52$), this layer supports only fundamental TE and TM waveguide modes, with mode indices of about 1.55. Note that in this respect our lasers are fundamentally different from the plasmon particle array lasers studied in Refs. [8,9,13,14], which use layer stacks that are index matched, hence relying on surface lattice resonances instead of waveguide modes.

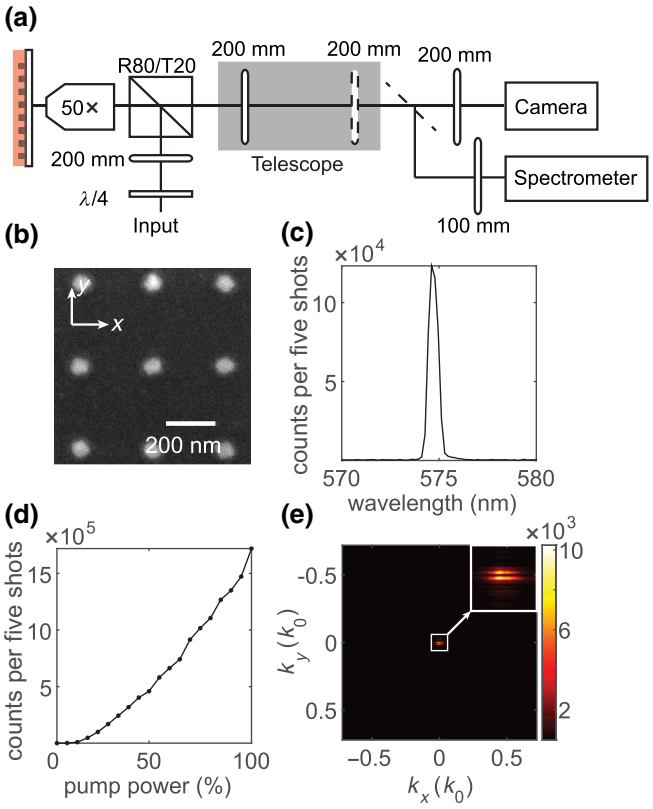

FIG. 2. (a) A schematic of the fluorescence microscope. We form either a real or a Fourier-space image on either a CCD or a spectrometer entrance slit. The first telescope lens (left) acts as a Fourier lens when the second lens (right, dashed) is removed. (b) A scanning-electron-micrograph (SEM) image of an 80 nm Ag particle array before depositing the gain medium. (c) A typical above-threshold emission spectrum at 50% pump power (80×80 μm^2 plasmon DFB laser with particle diameter 80 nm). (d) The corresponding threshold curve and (e) the Fourier image of the x-polarized emission, showing a narrow directional beam. The inset of (e) shows an enlargement near $k_x = k_y = 0$.

IV. CHARACTERIZATION MEASUREMENTS

Previously, we have reported lasing only for square arrays [12]. Therefore, we first confirm that rectangular arrays also lase. Figures 2(c)–(e) show data for a 80×80 μm^2 rectangular lattice of Ag disks with a diameter of 80 nm. When the pump intensity exceeds about 10% of the AOM range, the observed emission spectrum changes abruptly from the broad fluorescence spectrum of Rh6G to a narrow peak at around 575 nm, as shown in Fig. 2(c). The emission intensity in a narrow band (±1.5 nm) around the lasing wavelength as a function of

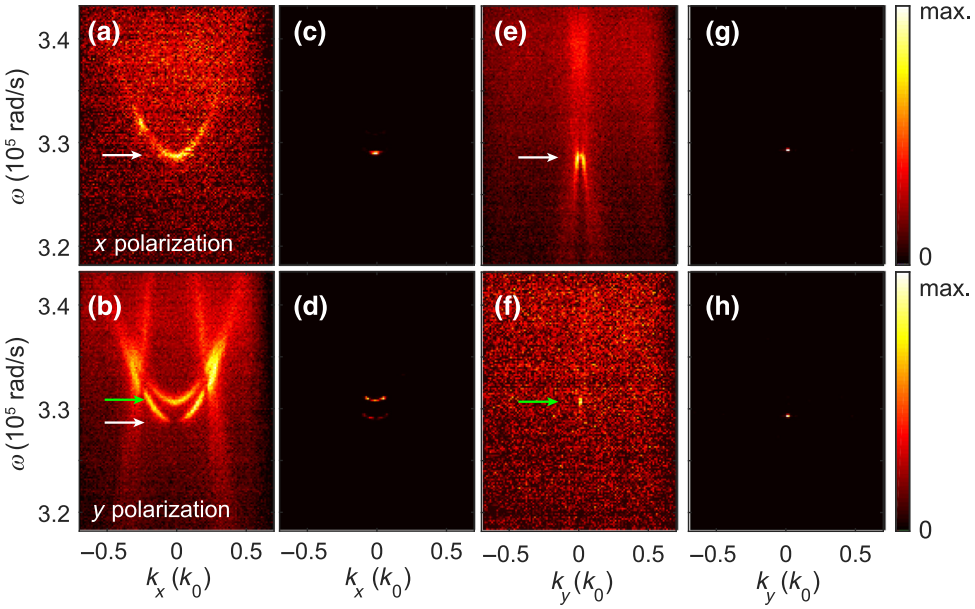

FIG. 3. The measured polarized Fourier spectra near (a)–(d) $k_y = 0$ and (e)–(h) $k_x = 0$: (a), (b), (e), and (f) below and (c), (d), (g), and (h) above threshold; (a),(c),(e),(g), x polarization; (b),(d),(f),(h), y polarization. Green arrows, TM waveguide mode; white arrows, TE. $L = 80\ \mu$m, $d = 90$ nm. Panels (a), (b), (e), and (f) are below-threshold (data from 600 shots at 5% pump power). Panels (c), (d), (g), and (h) show lasing at TE and TM band edges (OD1 neutral-density filter, single-shot excitation at 100% pump power). The maximum counts in each image are (a) 27, (b) 82, (c) 1670, (d) 3452, (e) 87, (f) 21, (g) 14 526, and (h) 632.

pump power [Fig. 2(d)] shows significantly different slopes before and after the 10% pump power level, indicating typical threshold behavior. Furthermore, when crossing the threshold, the laser output shows a strong change in directivity, from a Lambertian profile to a highly directional beam, as shown in Fig. 2(e). The observed bandwidth of about 1.5 nm is somewhat wider than the bandwidth of the typical plasmonic DFB lasers with a square lattice studied by Schokker *et al.* [12] [0.6 nm, measured with the same spectrometer and grating (300 lines/mm)]. We attribute this to the presence of multiple lasing modes with slightly different wave vectors and frequencies, as will be discussed in the following sections.

Spectrally resolved k-space imaging further characterizes the modes, as illustrated in Fig. 3 for a representative lasing array ($L = 80\ \mu$m, $d = 90$ nm). Figures 3(a), 3(b), 3(e), and 3(f) show below-threshold band diagrams for two different slices in k-space, i.e., at $k_y = 0$ and at $k_x = 0$, respectively, where we recall that the feedback direction for which a Bragg condition is satisfied is the y direction. The waveguide mode dispersion folded back in k-space by first-order Bragg diffraction hence appears as two anticrossing lines in the $k_x = 0$ plane and as a parabolic band in the $k_y = 0$ plane, as shown in Figs. 3(a), 3(b), 3(e), and 3(f). By measuring the polarization of the band diagram at $k_x = 0$ [Figs. 3(e) and 3(f)], we are able to separate the contributions of the TE (x polarization) and TM (y polarization) waveguide modes. Our data show that both fundamental TM (marked with green arrows) and TE (marked with white arrows) waveguide modes are supported by the sample, consistent with simple slab-waveguide dispersion calculations [49]. In Figs. 3(e) and 3(f), the TE feature appears strongest, while the TM waveguide mode leaves only a weak signature in fluorescence, consistent with the poor overlap of the TM waveguide mode (weak in-plane electric field) and the predominantly in-plane polarizability tensor of the flat disk nanoparticles.

The above-threshold images in Figs. 3(c), 3(d), 3(g), and 3(h) show that the sample lases near band edges of both TE and TM waveguide modes with two distinct frequencies. Unlike square-array lasers, which lase at $k_x \approx k_y \approx 0$, our rectangular-array lasers lase at $k_y \approx 0$ over a range of k_x values. The TM waveguide mode lases only in y polarization. This is consistent with Figs. 3(a) and 3(b), which show that the TM waveguide mode is polarized in the y direction, with hardly any x polarization components. The TE waveguide mode lasing output has, instead, x polarization components for all (small) k_x and, additionally, y polarization components for $k_x \neq 0$. Very similar behavior is observed for samples with different array sizes ($80 \times 80\ \mu$m^2, $60 \times 60\ \mu$m^2 and $40 \times 40\ \mu$m^2) and particle diameters (40–90 nm). All the investigated arrays lase in the TE mode, with both x and y polarization components, while only arrays with big particle diameters (larger than 70 nm) show lasing in the TM waveguide mode within the range of pump intensities. In the remainder of this paper, we focus on analyzing the TE mode only.

V. THE SPATIAL INTENSITY DISTRIBUTION AND COUPLING STRENGTH OF PLASMON DFB LASERS

To test whether the lasers indeed have a nontrivial spatial intensity distribution as predicted by CWT, we measure above-threshold real-space images in two detection polarization channels, as shown for a representative example in Fig. 4 ($60 \times 60\ \mu$m, lasing on TE mode). The lasing emissions in both detection polarization channels show very

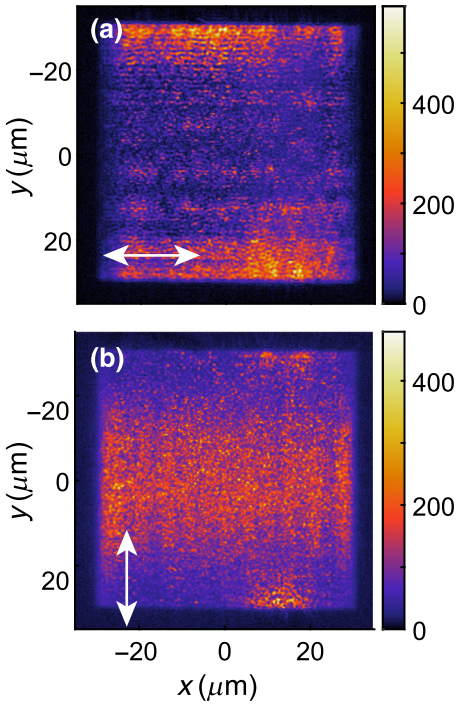

FIG. 4. Measured real-space profiles of a laser with $L = 60\ \mu$m, $d = 90$ nm in (a) x and (b) (y) polarization. Single shot, 100% pump power.

finely spaced intensity fluctuations, i.e., speckles that have a size at the diffraction limit of our imaging system, which in itself evidences spatial coherence [42]. The speckle pattern is multiplied by a slowly varying envelope that is hardly varying in the x direction, but that shows significant contrast as a function of the y coordinate. The x-polarized component has low intensity in the center ($y = 0$) and high intensity at the edges of the array, similar to either the coupled-mode prediction for an undercoupled symmetric mode or, alternatively, the profile of an asymmetric mode in any coupling-strength regime. The y-polarization component has the highest intensity at $y = 0$, which points uniquely to an overcoupled mode.

We measure the spatial intensity distribution in the feedback direction (the y direction) for the TE modes for all our samples by imaging the lasing array onto the spectrometer slit, selecting a slice from the center ($x \approx 0$) of the array along the y axis. The spectral dispersion of the spectrometer allows us to extract the spatial intensity distribution along the slice of sample selected by the entrance slit at any wavelength. By summing the intensity in a bandwidth within just 1 nm near the TE lasing wavelength from spectral images, we obtain the spatial intensity distribution in the y direction for the two polarizations of the TE mode. Selecting this small wavelength range also rules out any significant contribution of spontaneous emission, as the fluorescence spectrum of Rh6G has a width above 60 nm. Figures 5(a) and 5(b) show the measured spatial intensity distributions from samples with different particle sizes and field sizes for both detection polarization channels. Apart from the submicron intensity fluctuation (speckles), the x- and y-polarization components have distinctly different envelope functions. In all cases, the x-polarized laser emission has near-zero intensity (given the noise floor of our single-shot CCD images) in the center of the sample and highest intensity at the edges, as shown in Fig. 5(a). On the other hand, the y-polarized emission [Fig. 5(b)] shows a clear transition from an undercoupled profile with low intensity in the center from arrays with a small width (bottom row) or small particles (right column), to critically coupled profiles (center row and center column), and eventually to an overcoupled profile with an intensity that is higher in the center than at the edges as the array width and particle diameter increase to 80 μm and 90 nm (top left). Therefore, we conclude that the TE lasing mode is an antisymmetric combination of forward and backward waves, which in the far field carries over to an antisymmetric x-polarization component and a symmetric y-polarization signature. This assignment agrees with the conclusion in Ref. [48] that the lasing of the TE mode occurs at the band edge, where the nodes of the standing wave formed by the counterpropagating TE modes are at the nanoparticles, which is the configuration that minimizes absorption and radiation losses. These results are also consistent with the lasing profiles measured by Hakala *et al.* [14]. In Ref. [14], Hakala *et al.* claimed to observe lasing at two opposing stop-band edges, with a "dark" mode with low intensity in the center of the array and a "bright" mode with high intensity in the center. We note that, strictly, their observation neither provides a unique symmetry assignment that requires polarization resolution nor is unique for plasmonic "bright" dipole and "dark" quadrupole moments. Instead, these spatial profiles can occur for dielectric and plasmonic lasers alike according to CWT. Thus the apparent signature of being dark in the center of the array can be observed at both "dark" and "bright" dispersion branches, depending on the detection polarization with respect to the dominant lasing polarization, and is not exclusively indicative of whether the laser is operating in the undercoupled or the overcoupled regime.

Having established the symmetries of the different polarization channels, we compare the measured spatial intensity distributions with CWT and extract the apparent coupling strength κ through a fitting procedure. At a fixed particle size but different array sizes, we expect fixed values of the coupling strength κ so that different array sizes ($L = 80\ \mu$m, 60 μm, and 40 μm) allow us to verify the predicted influence on the spatial intensity distribution patterns according to Eqs. (2)–(3). As the coupling strength is only dependent on the size of the nanoparticles, we fit the data from all samples with the same particle diameter but different field sizes and polarizations simultaneously. Next, we expect that different coupling-strength values

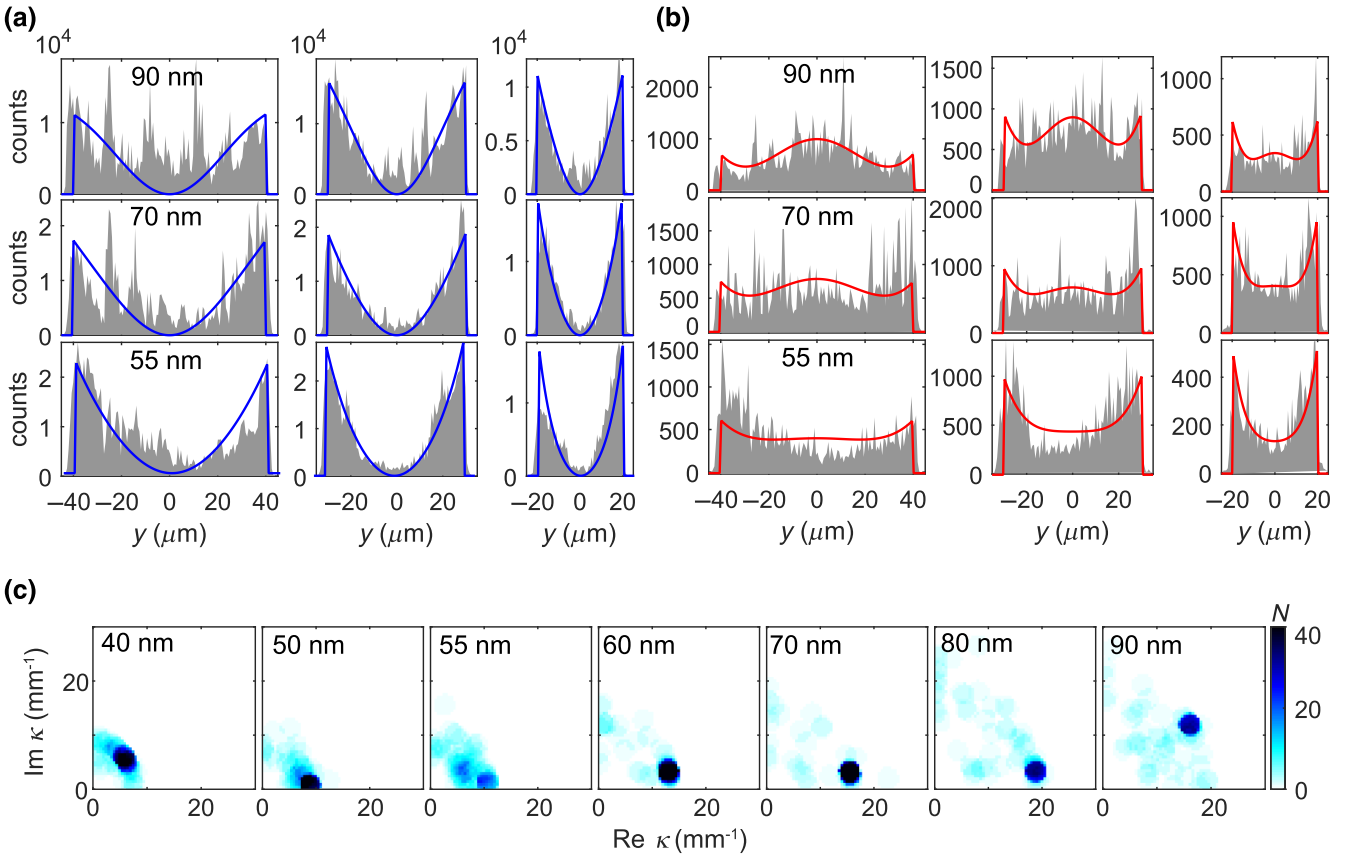

FIG. 5. The measured lasing intensity (gray) as a function of y from samples with different particle sizes (columns) and field sizes (rows), with the fits (blue) superimposed: (a) x polarization; (b) y polarization. The x-polarization results always show antisymmetric profiles. The y-polarization results show a transition from the undercoupled to the overcoupled regime. The samples are excited by single shots, at around 6 times the threshold power. (c) We obtain values of κ by fitting to the measured spatial intensity profiles of arrays with different particle sizes, using different starting points for the fit. The color scale represents the result of histogramming the resulting fit values, with the histogram entries weighted by the associated residual of the fit.

are obtained as a function of the particle diameter (40 to 90 nm). To perform the fit, we consider the solution of Eq. (3) for the lowest-threshold mode and extract a unique mapping from the coupling coefficient κ to γ. By fitting Eq. (2) to the experimental result, we obtain γ, which then translates into κ through the tabulated mapping. Note that this leaves some ambiguity since γ and $-\gamma$ are equivalent in the definition Eq. (2), while the intensity observables $|R \pm S|^2$ are agnostic to $\gamma \to \gamma^*$. Hence, we in fact determine $|\mathrm{Re}\,\kappa|$ and $|\mathrm{Im}\,\kappa|$.

It is difficult to obtain robust fits of the envelope functions using least-squares minimization due to the random speckles, which are effectively high-amplitude and high-spatial frequency noise that does not follow a Gaussian distribution. The blue and red solid lines in Figs. 5(a) and 5(b) show examples of fits, where all panels on the same row have been fitted simultaneously to a single parameter set. While there are some clear differences related to the speckle, overall the fitted curves represent the measured intensity envelopes well. As a check of the fit procedure, we run it with different starting values for κ evenly distributed in the first quadrant of the complex space within $|\kappa| < 0.03\ \mu\mathrm{m}^{-1}$ (undercoupled to overcoupled regime). Although the fit routine reports convergence at different values depending on the starting estimate, the lowest-residual results cluster in small regions in the complex plane. To determine the best global parameter estimate, we histogram the fitted values in discrete boxes in κ-space of 2 mm^{-1} width. Figure 5(c) shows the resulting 2D histogram in the complex plane. The fitted κ cluster at distinct complex values, with $|\kappa|$ increasing with increasing particle size, as expected from the fact that larger Ag particles scatter more strongly. As the best estimate for κ, we take the average of values in the densest bin.

Figure 6(a) shows that the coupling constant $|\kappa|$ according to our measurement ranges from 5 to 20 mm^{-1}, i.e., $|\kappa/k_0| \approx 0.0003$–$0.0012$, with a systematic variation in the magnitude and phase of κ with particle size. These variations are not monotonic in, e.g., particle volume, which is qualitatively consistent with the fact that the

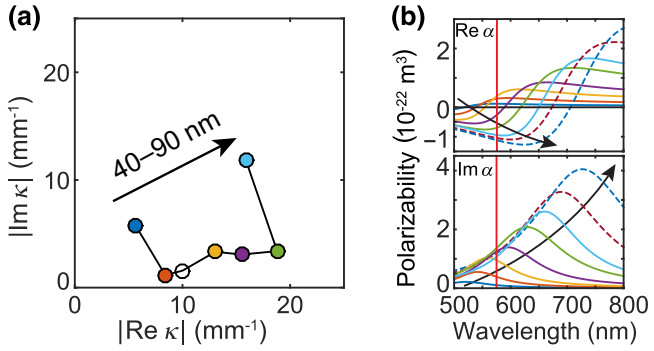

FIG. 6. (a) The value of κ for different particle diameters obtained by averaging over the densest bin (averaging radius of 2 mm^{-1}) in Fig. 5(c). The arrow indicates the increase of the particle diameter from 40 to 90 nm. (b) The real and imaginary parts of polarizability α as extracted by fitting extinction calculations (taken from Fig. 1b, Ref. [48]), Fig. 1b, for particle diameters of 40–110 nm (in 10 nm steps; dashed lines for particle sizes not included in this experiment). The color coding of points in (a) matches the lines in (b). The red vertical line is the lasing condition at 575 nm.

particle response as quantified by its polarizability is dispersive, with its dispersive line shape sweeping through the laser condition as the particle size is varied [Fig 6(b)]. In magnitude, the fitted κ values are similar to those in conventional index-coupled DFB lasers [44] (0–20 mm^{-1}) and, surprisingly, are much lower than expected from complex-coupled DFB lasers (50–200 mm^{-1}) with metal gratings [50]. Also, these values are significantly smaller than those observed for surface plasmon lasers ($\kappa/k_0 =$ 0.012–0.017) based on metal hole arrays [4,5]. This is highly surprising because plasmonic lattice lasers have been reported to benefit from the strong coupling between light and metal nanoparticles [9,42]. While holes in a metal film are not resonant scatterers, the metal nanoparticles in plasmon lasers have large resonant-scattering cross sections. Intuitively, one would hence expect plasmon particle arrays to have higher coupling coefficients than metal hole arrays, opposite to the experimental findings.

VI. INTERPRETATION OF THE FITTED COUPLING COEFFICIENTS

In this section, we examine the values of the measured coupling coefficients from two perspectives. The first perspective derives from the fact that according to the standard derivation of CWT (Sec. II), the coupling coefficients simultaneously determine the real-space profiles *and* the anticrossings in the photonic band structures. More particularly, κ in CWT directly determines the relative bandwidth of the stop gap in below-threshold band diagrams, while the magnitude of κ_{out} determines if the stop gap is asymmetric around the geometrical Bragg condition. Section V1 A examines the band structure. The second perspective is to compare measured coupling strengths to estimates of coupling coefficients from the geometry of our lasers using formulas common for (dielectric) DFB lasers [44] (Sec. V1 B).

A. The coupling coefficients and band structure

Earlier reports on plasmon-lattice lasers claimed a 3% relative stop-gap width in band structures. Hence one would expect $|\kappa/k_0| \approx 0.03$ instead of 0.0012. Here, we compare the fitted values of $\mathrm{Re}\,(\kappa)/G_y$ with the band-edge shifts measured from the investigated lasers, as well as those extracted from earlier work [12,48]. We extract TE band edges from the below-threshold emission spectra of the lasers at $k_x = k_y = 0$ (averaging over $|k_y| < 0.02k_0$ at $k_x = 0$) in x-polarized Fourier spectral images, shown as the color scale in Fig. 7(a). The spectral peaks are identified as two stop-band edges [center frequencies plotted in Fig. 7(c)]. This band, with its narrow bandwidth, corresponds to the asymmetric lasing mode with nodes at the metal nanoparticles. The lower band edge has a much broader bandwidth and shifts significantly toward the red as the particle diameter increases from 40 to 50 nm, and then disappears due to broadening as the particle size increases further. We also simulate near-normal incidence transmission using the finite-element method (FEM) method (via the COMSOL multiphysics software [51]), taking 30-nm-height Ag cylinders [52] on glass ($n = 1.50$) and in a $n = 1.60$ slab of thickness 350 nm. We choose slightly off-normal incidence (angle below 0.5°), as otherwise the coupling to the narrow band edge is forbidden by symmetry. The transmission [color scale in panel 7(b)] again shows distinct resonances, with a narrow band that hardly shifts and a lower band that redshifts and broadens with increasing particle size. The broadening of the lower band indicates increasing ohmic and radiative losses, which may explain its vanishing in the fluorescence data. The small, approximately 0.3×10^{15} rad/s, shift in frequencies between measurement and simulations is likely due to a small difference in the waveguide-mode index. The band at $\omega \sim 3.4 \times 10^{15}$ rad/s is a surface lattice resonance at the SU8-glass interface, which is irrelevant to the lasing experiment.

Figure 7(c) shows the shifts of the measured band edges from the theoretical band crossing point $\omega_0 = c/n_{WG}G_y$. To construct a "master diagram" that can also accommodate literature data sets alongside our measurements and that explicitly accounts for the plasmonic resonance of the particles, we convert the particle size into a detuning parameter. This normalized detuning is defined as the difference between the lasing frequency and the single-particle plasmon resonance frequency [denoted ω_{LPSR}, for localized surface plasmon resonance (LSPR)], divided

by the single-particle plasmon resonance width (denoted Γ_{LSPR}). The single-particle properties are derived from scattering calculations [Fig. 6(b), Ref. [48]]. Alongside the band shifts in this work [closed blue and red points in Fig. 7(c)], band-edge shifts are shown for square lattices with the same gain medium as studied in this work, but much larger particles (Ref. [12], open diamonds) and samples with the lasing condition tuned far into the red by using a larger pitch and a different gain medium (open circles [48]). The three data sets together cover red detuning [48], near-zero detuning, and blue detuning [12] and show important general features. The stop gap has one band edge that barely shifts from the geometric Bragg diffraction condition and one band edge that shifts strongly. The shifting band shows a strong dependence on detuning from the plasmon resonance, commensurate with the fact that it corresponds to the symmetric Bloch mode, with field antinodes overlapping strongly with the particles. Notably, the shift increases when approaching the plasmon resonance and its sign reverses at zero detuning. This behavior qualitatively traces out the real part of the dispersive particle polarizability. The band that hardly shifts corresponds to the antisymmetric mode with nodes at the particles, which is also the mode that lases in the experiments. As earlier work [48] only examined the relative stop-gap width [Fig. 7(d)], it overlooked the large asymmetry in the two band shifts relative to ω_0.

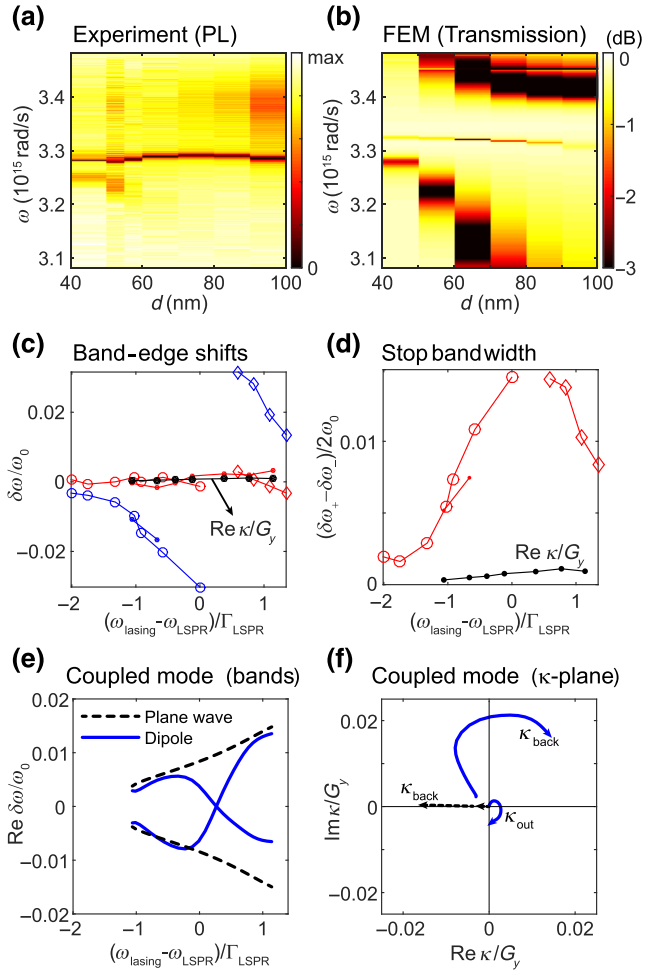

FIG. 7. (a) Measured below-threshold emission spectra versus the particle diameter, near normal incidence. (b) The zero-order transmittance obtained from FEM simulation. (c) The shift of the band edges (red, lasing band edge; blue, nonlasing band edge) relative to the Bragg condition, versus the detuning between the lasing condition and the plasmon resonance. This graph combines data from this work (closed symbols) and Refs. [12,48] (open symbols). The closed black symbols show the coupling constant $\mathrm{Re}\,\kappa/G_y$ (black) from Fig. 6. (d) The measured (half-)band-gap width [red, the difference between the red and blue points in panel (c)], alongside $\mathrm{Re}\,\kappa/G_y$ (black). (e) The band shift and (f) the coupling coefficients from CWT [black dashed curves, Eqs. (4) and (5)] and the dipole approximation [blue solid curves, Eqs. (8) and (9)]. The arrows indicate increasing particle size.

The coupling strength $|\mathrm{Re}\,\kappa|/G_y$ that we derive from fitting the real-space laser intensity profiles stays far below the half width of the band gap, and is similar in magnitude to the very small shift in frequency of the lasing band edge rather than to the stop-gap width. This observation is surprising in the framework of CWT. In CWT, strongly asymmetric band shifts require $|\mathrm{Im}\,\kappa_{out}| \gg |\mathrm{Re}\,\kappa_{back}|$. Yet if this inequality were indeed to hold, the coupling strength evident in real-space intensity distributions would be much larger than we observe and would far exceed the shift of the upper band. Conversely, the negligible shift of the lasing band edge and the small coupling strength obtained from real-space profiles according to CWT dictate a negligible contribution of κ_{out}, incommensurate with the overall stop-gap width. We conclude that the standard CWT fails to describe plasmon particle lasers consistently. The parameters needed to parametrize real-space intensity distributions are not reconcilable with the plasmon band structure. We ascribe this to the fact that standard CWT assumes a perturbative plane-wave expansion framework, which accounts very poorly for the resonant and highly localized nature of the metal particles. This problem is also well known from the convergence problems encountered by plane-wave-based calculation methods for metal gratings [53]. At the same time, even if CWT fails to capture the band shifts, the fact that the lasing band shows an anomalously small shift is consistent with the coupling strength evident in the real-space intensity distributions.

B. Geometry-based estimates

As a second perspective on the measured coupling strengths, we compare with estimates of the coupling coefficients derived from the geometry of our lasers. For a waveguide geometry with dielectric perturbation and in the limit of particles much smaller in height than the scale

on which the waveguide mode varies, the formalism of Kazarinov *et al.* [44] results in

$$\kappa_{\text{back}} \approx \left(\frac{1}{2G_y}\right)\left(\frac{\omega}{c}\right)^2 \varepsilon_{02}(z_0)\phi(z_0)^2 h / \int \phi(z)^2 dz, \quad (4)$$

$$\kappa_{\text{out}} \approx -\left(\frac{1}{4G_y^2}\right)\left(\frac{\omega}{c}\right)^4 (\varepsilon_{01}(z_0)\phi(z_0))^2 h^2 / \int \phi(z)^2 dz. \quad (5)$$

Here, $h = 30$ nm is the thickness of the particles, $z_0 = 15$ nm is the height of the particle center, and ε_{mn} signifies the 2D Fourier coefficient [at $(m,n)2\pi/d$] of the relative permittivity of the scattering particles embedded in the waveguide background. The vertically stratified structure causes a weighting of the Fourier coefficients by the waveguide-mode profile $\phi(z)$. The above expressions do not naturally relate to, e.g., the resonant dipole polarizability α of the localized plasmon scatterers. We turn Eq. (5) into one that does include α by following the approach of Spry and Kosan [54] and Vos *et al.* [55,56] in the field of colloidal photonic crystals. Vos *et al.* [55,56] introduced a "photonic strength" Ψ that equals the relative stop-gap width $(\Delta\omega/\omega)$ and that for a 3D photonic crystal of spheres of radius R and polarizability α is expressed as

$$\Psi = 4\pi \frac{\alpha}{V} f(GR) \quad \text{with } f(x) = \frac{j_1(x)}{x}. \quad (6)$$

This result is also well known in dynamical x-ray diffraction theory (in the limit of very small polarizabilities) [57]. In this equation, V is the unit-cell volume, $\alpha = 3V_{\text{sphere}}(\varepsilon_{\text{sphere}} - \varepsilon_{\text{host}})/4\pi(\varepsilon_{\text{sphere}} + 2\varepsilon_{\text{host}})$, and $f(GR)$ is proportional to the Fourier transform of a sphere, with j_n the spherical Bessel function of the first kind, and G the length of the reciprocal lattice vector that causes the stop gap. The plane-wave method for photonic crystals instead predicts [58]

$$\frac{\Delta\omega}{\omega} = \frac{\varepsilon_G}{\bar{\varepsilon}} = \frac{\varepsilon_{\text{sphere}} - \varepsilon_{\text{host}}}{\bar{\varepsilon}} \frac{4\pi R^3}{V} f(GR), \quad (7)$$

where ε_G is the Fourier transform of the relative permittivity and $\bar{\varepsilon}$ is the volume-averaged relative permittivity. Note that Eq. (6) is different from Eq. (7), unless one substitutes $\alpha = 3V_{\text{sphere}}(\varepsilon_{\text{sphere}} - \varepsilon_{\text{host}})/4\pi(\varepsilon_{\text{sphere}} + 2\varepsilon_{\text{host}})$ for $V_{\text{sphere}}(\varepsilon_{\text{sphere}} - \varepsilon_{\text{host}})/4\pi\bar{\epsilon}$. Nonetheless, empirically Eq. (6) is a better predictor for band gaps in high-index photonic crystals than Eq. (7), suggesting that Eq (6) accounts better for strong multiple scattering. Equation (6) can be read as an ansatz to convert Eqs. (4) and (5). To this end, we evaluate the Fourier coefficients ϵ_{01} and ϵ_{02} and replace any occurrence of $(\epsilon_{\text{disk}} - \epsilon_{\text{SU8}})/n_{\text{WG}}^2 V$ with $4\pi\alpha$, leading to

$$\frac{\kappa_{\text{back}}}{G_y} = \frac{4\pi\alpha}{V_{\text{eff}}} f(2GR), \quad (8)$$

$$\frac{\kappa_{\text{out}}}{k} = -kh_{\text{eff}}\left(\frac{4\pi\alpha}{V_{\text{eff}}} f(GR)\right)^2, \quad \text{with } f(x) = \frac{J_1(x)}{x}. \quad (9)$$

Now, the cylindrical Bessel function J_n appears and the effective unit-cell volume V_{eff} is the product of the unit-cell area and an effective waveguide-mode height $h_{\text{eff}} = \int |\phi(z)|^2 dz / |\phi(z_0)|^2$.

Figures 7(e) and 7(f) show the expected coupling constants and band shifts using both the "plane-wave" result [Eqs. (4) and (5)] and the modified "dipole" result [Eq. (9)]. For evaluation, we use the polarizability at fixed wavelength (575 nm, the lasing wavelength) as extracted by matching to full-wave simulations for Ag particles in the glass-SU8-air system [Fig. 6(b)]. In both models, κ_{out} is much smaller than κ_{back} and $|\kappa_{\text{back}}/G_y|$ reaches about 0.02, quite similar to the 3% relative stop-gap width in Figs. 7(c) and 7(d), but exceeding by one order of magnitude the coupling coefficient obtained from real-space intensity distributions. The major difference between the two models lies in the phase of the coupling coefficients, as only the dipole model captures the resonant dispersive behavior of α. On a positive note, the model that uses the dipole polarizability well captures the dispersive behavior of the band-edge shifts and the nonmonotonic increase of the coupling coefficient with particle size. However, there remains an important difference with the data, since both models predict symmetric shifts around the Bragg condition, as opposed to the observed nonshifting band.

To conclude, as has also been observed for metal hole array lasers [4,5], CWT parametrizes the spatial intensity distributions in plasmon-lattice lasers. However, in contrast to the behavior of conventional DFBs as well as metal hole array lasers, the actual parameter values are neither internally consistent with the stop gaps observed in the band structures nor reconcilable with simple estimates on the basis of the unit-cell geometry. The common assumption underlying these consistency checks is that CWT with its parameters can be derived from a plane-wave expansion method. However, plane-wave expansion methods are notoriously poor for metal nanoparticle gratings, providing a rationale for why CWT appears inconsistent with parameter estimates from geometry and with measured stop bands in band structures.

VII. CONCLUSION

In this paper, we quantify real-space intensity distributions in plasmon antenna array plasmon DFB lasers and

show that they can be well parametrized by the seminal CWT of Kogelnik and Shank [43]. Notably, we trace the transition from undercoupled to overcoupled behavior as a given particle-array geometry is scaled in overall field size L and we can extract coupling-strength parameters that only depend on the choice of unit cell (i.e., the particle size). This observation provides an alternative explanation for the results of Hakala *et al.* [14] who claimed that "bright" and "dark" lasing modes were associated with dipole and quadrupolar particle resonances. Instead, the same spatial profiles can arise from CWT as a combined result of detection polarization, mode symmetry, and the coupling strength, without resorting to any plasmonic-resonance feature.

While CWT forms an effective parametrization, the extracted coupling strengths are anomalously small and inconsistent with parameter-value estimates in the coupled-wave framework. Viewing CWT as a generic effective description of coupled forward and backward waves, it is not surprising that it provides an effective parametrization. However, the matching of this description to photonic-band-structure parameter estimates is essentially based on the assumption that the plane-wave expansion method, from which CWT derives, is accurate. Plane-wave approximations are notorious for performing poorly on strongly scattering plasmonic constituents [52]. The quantitative mismatch between the CWT coupling constants and the data hence points at a fundamental shortcoming of coupled-wave modeling for strongly scattering periodic active systems.

Our result should be read as a stimulus to develop new theory. Many researchers currently focus on collective effects, strong coupling, and exciton-polariton physics in plasmon lattices [3–13,13,14,14–19]. At the same time, active dielectric metasurfaces with gain are of increasing interest [20]. For all these systems, the unit cells are resonant and hence the problem that we identify is acute. Ideally, models to describe the physics of such systems should capture the unit-cell physics in real space. Currently available real-space models for such systems with gain do not incorporate noise to start the lasing process and use Floquet periodic boundary conditions. It is hence a formidable challenge to deal with finite systems. Our work provides clear observables against which a model should be benchmarked, namely (1) band structures with relative wide stop bands with asymmetric band shifts and (2) lasing thresholds with spatial intensity distributions mimicking CWT predictions, yet (3) with anomalous coupling coefficients compared to the band structure. In the absence of such a model, one could pragmatically—but without any first-principles footing—adopt CWT as a parametrization on the understanding that *different* effective coupling coefficients should be assigned to the two band edges. On the basis of the interpretation of Hakala *et al.* [14], one could speculate that a main challenge is to identify the coupling coefficients of various bands with multipolar particle resonances.

ACKNOWLEDGMENTS

We thank Sachin Kasture, Martin van Exter, Mohammed Ramezani, Alexei Halpin, and Jaime Gomez Rivas for insightful discussions, and are grateful to Dimitry Lamers and Bob Drenth for nanofabrication. Also, we thank Esther Alarcon Llado for suggestions to improve the manuscript. This work is part of the research program STW LEDMAP with project number 12754 which is (partly) financed by the Netherlands Organisation for Scientific Research (NWO). It was performed at the research institute AMOLF.

APPENDIX: SPATIAL COHERENCE

We confirm transverse spatial coherence using double-slit experiments. A pair of parallel slits is placed in the intermediate image plane (the center of the telescope, a $50\times$ magnified image of the sample). The slits are fabricated in chrome on glass (Delta Mask), with a width of 0.3 mm and a center-to-center distance of 3 mm. Using a cylindrical lens ($f = 20$ mm) and relay optics, we obtain a two-slit interference pattern at the camera or the spectrometer entrance plane. The resulting image is in one dimension a (magnified) Fourier transform of the product of laser emission and slits, and has a spatial coordinate along the slit axis as the horizontal coordinate. For full coherence and on the proviso of equal intensity through the slits, the image will have a fringe pattern in the y (k_y) direction that follows

$$I(k_y) \propto \frac{\sin^2(k_y W/2)}{k_y^2} \cdot [1 + \cos(k_y D)], \tag{A1}$$

where W is the slit width and D is the slit distance. If the laser emissions selected by the two slits are only partially coherent with each other, a reduced fringe contrast v results:

$$v = \frac{I_{\max} - I_{\min}}{I_{\max} + I_{\min}}. \tag{A2}$$

Taking the 80 μm $\times$ 80 μm lasers as a representative example, we measure the coherence between two 6-μm-wide slices that are 60 μm apart, each positioned near one edge of the sample. We take care to balance the emission intensities by placing the slits symmetrically. Figures 8(a) and 8(b) show the x-polarized interference images measured with the CCD camera from the laser with particle diameter $d = 90$ nm, with the x (respectively, the y) direction of the laser aligned along the direction of the slits, respectively. Clear interference fringes are only observed when the slit pair is oriented parallel to the x-direction, meaning that interference is recorded from two stripes displaced along the y-coordinate, i.e., the coordinate that is

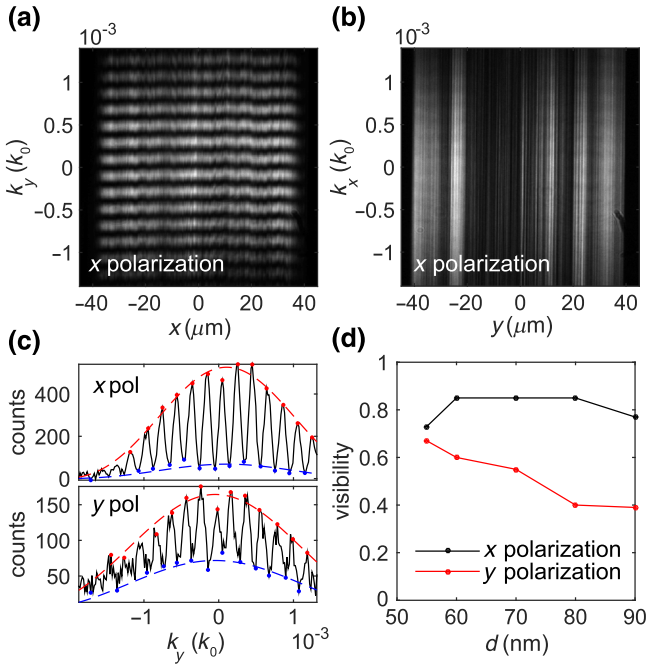

FIG. 8. (a),(b) Double-slit interference patterns for x polarization with slits parallel to (a) the x direction and (b) the y direction. (c) Double-slit interference patterns for (upper) x and (lower) y polarizations at the wavelength of the TE lasing mode, with peaks and valleys fitted to two sinc functions. (d) The visibilities of the x and y polarization of the TE mode obtained from the fit for lasers with different particle sizes. Laser size: 80 μm × 80 μm. (a)–(c): $d = 90$ nm.

responsible for laser feedback. This indicates a strong spatial coherence in the y direction, consistent with CWT for a laser with feedback along y only. To deduce the fringe contrast, we eliminate the influence of the spontaneous emission background and the TM waveguide mode of the lasers by spectral selection using the spectrometer. Figure 8(c) shows an example of a resulting spectrally filtered interference pattern ($d = 90$ nm laser, slice near $x = 0$) in two different polarization channels. Fitting the peaks and valleys with sinc functions [motivated by Eq. (A1)], we obtain the fringe visibility. In x polarization, we find a visibility around 0.8, i.e., high coherence for all measured lasers. We attribute the fact that the measured visibility is below 1 mainly to the fact that any unbalance in the emission intensity transmitted through each slit reduces visibility, as may be caused by speckles or small misalignments. The y polarization has a visibility that reduces from 0.7 to 0.4 as the particle size increases from 55 to 90 nm (from the undercoupled to the critically coupled regime). We expect this reduced contrast to reflect the fact that the y-polarized laser emission is generally weaker (for the TE mode), so that at any given background level, the fringe contrast is less than for x polarization. Indeed, the background is similar for the two polarizations in (c) (blue curve).

[1] V. G. Kravets, A. V. Kabashin, W. L. Barnes, and A. N. Grigorenko, Plasmonic surface lattice resonances: A review of properties and applications, Chem. Rev. **118**, 5912 (2018).

[2] G. Lozano, S. R. K. Rodriguez, M. A. Verschuuren, and J. G. Rivas, Metallic nanostructures for efficient LED lighting, Light: Sci. Appl. **5**, e16080 (2016).

[3] F. van Beijnum, P. J. van Veldhoven, E. J. Geluk, M. J. A. de Dood, G. W. 't Hooft, and M. P. van Exter, Surface plasmon lasing observed in metal hole arrays, Phys. Rev. Lett. **110**, 206802 (2013).

[4] M. P. van Exter, V. T. Tenner, F. van Beijnum, M. J. A. de Dood, P. J. van Veldhoven, E. J. Geluk, and G. W. 't Hooft, Surface plasmon dispersion in metal hole array lasers, Opt. Express **21**, 27422 (2013).

[5] V. T. Tenner, M. J. A. de Dood, and M. P. van Exter, Measurement of the phase and intensity profile of surface plasmon laser emission, ACS Photonics **3**, 942 (2016).

[6] X. Meng, J. Liu, A. V. Kildishev, and V. M. Shalaev, Highly directional spaser array for the red wavelength region, Laser Photonics Rev. **8**, 896 (2014).

[7] J. Stehr, J. Crewett, F. Schindler, R. Sperling, G. von Plessen, U. Lemmer, J. M. Lupton, T. A. Klar, J. Feldmann, A. W. Holleitner, M. Forster, and U. Scherf, A low threshold polymer laser based on metallic nanoparticle gratings, Adv. Mater. **15**, 1726 (2003).

[8] J. Y. Suh, C. H. Kim, W. Zhou, M. D. Huntington, D. T. Co, M. R. Wasielewski, and T. W. Odom, Plasmonic bowtie nanolaser arrays, Nano Lett. **12**, 5769 (2012).

[9] W. Zhou, M. Dridi, J. Y. Suh, C. H. Kim, D. T. Co, M. R. Wasielewski, G. C. Schatz, and T. W. Odom, Lasing action in strongly coupled plasmonic nanocavity arrays, Nat. Nanotechnol. **8**, 506 (2013).

[10] A. Yang, T. B. Hoang, M. Dridi, C. Deeb, M. H. Mikkelsen, G. C. Schatz, and T. W. Odom, Real-time tunable lasing from plasmonic nanocavity arrays, Nat. Commun. **6**, 6939 (2015).

[11] A. Yang, Z. Li, M. P. Knudson, A. J. Hryn, W. Wang, K. Aydin, and T. W. Odom, Unidirectional lasing from template-stripped two-dimensional plasmonic crystals, ACS Nano **9**, 11582 (2015).

[12] A. H. Schokker and A. F. Koenderink, Lasing at the band edges of plasmonic lattices, Phys. Rev. B **90**, 155452 (2014).

[13] M. Ramezani, A. Halpin, A. I. Fernández-Domínguez, J. Feist, S. R.-K. Rodriguez, F. J. Garcia-Vidal, and J. G. Rivas, Plasmon-exciton-polariton lasing, Optica **4**, 31 (2017).

[14] T. K. Hakala, H. T. Rekola, A. I. Väkeväinen, J.-P. Martikainen, M. Necada, A. J. Moilanen, and P. Törmä, Lasing in dark and bright modes of a finite-sized plasmonic lattice, Nat. Commun. **8**, 13687 (2017).

[15] H. T. Rekola, T. K. Hakala, and P. Törmä, One-dimensional plasmonic nanoparticle chain lasers, ACS Photonics **5**, 1822 (2018).

[16] K. S. Daskalakis, A. I. Väkeväinen, J.-Petri Martikainen, T. K. Hakala, and P. Törmä, Ultrafast pulse generation in

an organic nanoparticle-array laser, Nano Lett. **18**, 2658 (2018).
[17] S. R. K. Rodriguez, Y. T. Chen, T. P. Steinbusch, M. A. Verschuuren, A. F. Koenderink, and J. G. Rivas, From weak to strong coupling of localized surface plasmons to guided modes in aluminescent slab, Phys. Rev. B **90**, 235406 (2014).
[18] A. I. Väkeväinen, R. J. Moerland, H. T. Rekola, A.-P. Eskelinen, J.-P. Martikainen, D.-H. Kim, and P. Törmä, Plasmonic surface lattice resonances at the strong coupling regime, Nano Lett. **14**, 1721 (2014).
[19] T. K. Hakala, A. J. Molainen, A. I. Väkeväinen, R. Guo, J.-P. Martikainen, K. S. Daskalakis, H. T. Rekola, A. Julku, and P. Törmä, Bose-Einstein condensation in a plasmonic lattice, Nat. Phys. **14**, 739 (2018).
[20] S. T. Ha, Y. Hsing Fu, N. K. Emani, Z. Pan, R. M. Bakker, R. Paniagua-Domínguez, and A. I. Kuznetsov, Directional lasing in resonant semiconductor nanoantenna arrays, Nat. Nanotechnol. 13, 1042 (2018).
[21] D. J. Bergman and M. I. Stockman, Surface plasmon amplification by stimulated emission of radiation: Quantum generation of coherent surface plasmons in nanosystems, Phys. Rev. Lett. **90**, 027402 (2003).
[22] J. B. Khurgin, Prospects and merits of metal-clad semiconductor lasers from nearly UV to far IR, Opt. Express **23**, 4186 (2015).
[23] R. F. Oulton, V. J. Sorger, T. Zentgraf, R.-M. Ma, C. Gladden, L. Dai, G. Bartal, and X. Zhang, Plasmon lasers at deep subwavelength scale, Nature **461**, 629 (2009).
[24] X. Meng, A. V. Kildishev, K. Fujita, K. Tanaka, and V. M. Shalaev, Wavelength-tunable spasing in the visible, Nano Lett. **13**, 4106 (2013).
[25] M. I. Stockman, The spaser as a nanoscale quantum generator and ultrafast amplifier, J. Opt. **12**, 024004 (2010).
[26] D. A. Genov, R. F. Oulton, G. Bartal, and X. Zhang, Anomalous spectral scaling of light emission rates in low-dimensional metallic nanostructures, Phys. Rev. B **83**, 245312 (2011).
[27] T. P. H. Sidiropoulos, R. Röder, S. Geburt, O. Hess, S. A. Maier, C. Ronning, and R. F. Oulton, Ultrafast plasmonic nanowire lasers near the surface plasmon frequency, Nat. Phys. **10**, 870 (2014).
[28] R.-M. Ma, R. F. Oulton, V. J. Sorger, G. Bartal, and X. Zhang, Room-temperature sub-diffraction-limited plasmon laser by total internal reflection, Nat. Mater. **10**, 110 (2011).
[29] M. T. Hill, Y.-S. Oei, B. Smalbrugge, Y. Zhu, T. de Vries, P. J. van Veldhoven, F. W. M. van Otten, T. J. Eijkemans, J. P. Turkiewicz, H. de Waardt, E. J. Geluk, S.-H. Kwon, Y.-H. Lee, R. Nötzel, and M. K. Smit, Lasing in metallic-coated nanocavities, Nat. Photonics **1**, 589 (2007).
[30] M. T. Hill, M. Marell, E. S. P. Leong, B. Smallbrugge, Y. Zhu, M. Sun, P. J. van Veldhoven, E. J. Geluk, F. Karouta, Y.-S. Oei, R. Nötzel, C.-Z. Ning, and M. K. Smit, Lasing in metal-insulator-metal sub-wavelength plasmonic waveguides, Opt. Express **17**, 11107 (2009).
[31] K. Yu, A. Lakhani, and M. C. Wu, Subwavelength metal-optic semiconductor nanopatch lasers, Opt. Express **18**, 8790 (2010).
[32] M. P. Nezhad, A. Simic, O. Bondarenko, B. Slutsky, A. Mizrahi, L. Feng, V. Lomakin, and Y. Fainman, Room-temperature subwavelength metallo-dielectric lasers, Nat. Photonics **4**, 395 (2010).
[33] J. H. Lee, M. Khajavikhan, A. Simic, Q. Gu, O. Bondarenko, B. Slutsky, M. P. Nezhad, and Y. Fainman, Electrically pumped sub-wavelength metallo-dielectric pedestal pillar lasers, Opt. Express **19**, 21524 (2011).
[34] M. Khajavikhan, A. Simic, M. Katz, J. H. Lee, B. Slutsky, A. Mizrahi, V. Lomakin, and Y. Fainman, Thresholdless nanoscale coaxial lasers, Nature **482**, 204 (2012).
[35] H. Kogelnik and C. V. Shank, Stimulated emission in a periodic structure, Appl. Phys. Lett. **18**, 152 (1971).
[36] B. E. Kruschwitz and T. G. Brown, Complex-coupled distributed feedback laser with negative differential coupling, Appl. Phys. Lett. **67**, 461 (1995).
[37] G. A. Turnbull, P. Andrew, M. J. Jory, W. L. Barnes, and I. D. W. Samuel, Relationship between photonic band structure and emission characteristics of a polymer distributed feedback laser, Phys. Rev. B **64**, 125122 (2001).
[38] G. Heliotis, R. D. Xia, G. A. Turnbull, P. Andrew, W. L. Barnes, I. D. W. Samuel, and D. D. C. Bradley, Emission characteristics and performance comparison of polyfluorene lasers with one- and two-dimensional distributed feedback, Adv. Funct. Mater. **14**, 91 (2004).
[39] I. D. W. Samuel and G. A. Turnbull, Organic semiconductor lasers, Chem. Rev. **107**, 1272 (2007).
[40] H. Matsubara, S. Yoshimoto, H. Saito, Y. Jianglin, S. Tanaka, and Y. Noda, GaN photonic-crystal surface-emitting laser at blue-violet wavelengths, Science **319**, 445 (2008).
[41] A. H. Schokker and A. F. Koenderink, Lasing in quasi-periodic and aperiodic plasmon lattices, Optica **3**, 686 (2016).
[42] A. H. Schokker and A. F. Koenderink, Statistics of randomized plasmonic lattice lasers, ACS Photonics **2**, 1289 (2015).
[43] H. Kogelnik and C. V. Shank, Coupled-wave theory of distributed feedback lasers, J. Appl. Phys. **43**, 2327 (1972).
[44] R. Kazarinov and C. Henry, Second-order distributed feedback lasers with mode selection provided by first-order radiation losses, IEEE J. Quantum Electron. **21**, 144 (1985).
[45] K. Sakai, E. Miyai, and S. Noda, Two-dimensional coupled wave theory for square-lattice photonic-crystal lasers with tm-polarization, Opt. Express **15**, 3981 (2007).
[46] M. Koba and P. Szczepanski, The threshold mode structure analysis of the two-dimensional photonic crystal lasers, Prog. Electromagn. Res. **125**, 365 (2012).
[47] Y. Liang, C. Peng, K. Sakai, S. Iwahashi, and S. Noda, Three-dimensional coupled-wave analysis for square-lattice photonic crystal surface emitting lasers with transverse-electric polarization: Finite-size effects, Opt. Express **20**, 15945 (2012).
[48] A. H. Schokker, F. van Riggelen, Y. Hadad, A. Alù, and A. F. Koenderink, Systematic study of the hybrid plasmonic-photonic band structure underlying lasing action of diffractive plasmon particle lattices, Phys. Rev. B **95**, 085409 (2017).

[49] H. P. Urbach and G. L. J. A. Rikken, Spontaneous emission from a dielectric slab, Phys. Rev. A **57**, 3913 (1998).

[50] M. Kamp, J. Hofmann, F. Schäfer, M. Reinhard, M. Fischer, T. Bleuel, J. Reithmaier, and A. Forchel, Lateral coupling as a material independent way to complex coupled DFB lasers, Opt. Mater. **17**, 19 (2001).

[51] COMSOL Multiphysics version 5.2. www.comsol.com. COMSOL AB, Stockholm, Sweden.

[52] P. B. Johnson and R. W. Christy, Optical constants of the noble metals, Phys. Rev. B **6**, 4370 (1972).

[53] L. Li and C. W. Haggans, Convergence of the coupled-wave method for metallic lamellar diffraction gratings, J. Opt. Soc. Am. A **10**, 1184 (1993).

[54] R. J. Spry and D. J. Kosan, Theoretical analysis of the crystalline colloidal array filter, Appl. Spectr. **40**, 782 (1986).

[55] W. L. Vos, R. Sprik, A. van Blaaderen, A. Imhof, A. Lagendijk, and G. H. Wegdam, Strong effects of photonic band structures on the diffraction of colloidal crystals, Phys. Rev. B **53**, 16231 (1996).

[56] W. L. Vos, M. Megens, C. M. van Kats, and P. Bösecke, Transmission and diffraction by photonic colloidal crystals, J. Phys.-Cond. Matt. **8**, 9503 (1996).

[57] W. H. Zachariasen, *Theory of X-Ray Diffraction in Crystals* (John Wiley and Sons, New York, 1945).

[58] H. S. Sözüer, J. W. Haus, and R. Inguva, Photonic bands: Convergence problems with the plane-wave method, Phys. Rev. B **45**, 13962 (1992).